MATERIALS SCIENCE

# Metal-carbide eutectics with multiprincipal elements make superrefractory alloys

**Qinqin Wei[1,2], Xiandong Xu[1]*, Qiang Shen[2]*, Guoqiang Luo[2], Jian Zhang[2], Jia Li[3], Qihong Fang[3], Chain-Tsuan Liu[4], Mingwei Chen[5]*, Tai-Gang Nieh[6]*, Jianghua Chen[1,7]***



**Materials with excellent high-temperature strength are now sought for applications in hypersonics, fusion reactors, and aerospace technologies. Conventional alloys and eutectic multiprincipal-element alloys (MPEAs) exhibit insufficient strengths at high temperatures due to low melting points and microstructural instabilities. Here, we report a strategy to achieve exceptional high-temperature microstructural stability and strength by introducing eutectic carbide in a refractory MPEA. The synergistic strengthening effects from the multiprincipal-element mixing and strong dislocation blocking at the interwoven metal-carbide interface make the eutectic MPEA not only have outstanding high-temperature strength (>2 GPa at 1473 K) but also alleviate the room-temperature brittleness through microcrack tip blunting by layered metallic phase. This strategy offers a paradigm for the design of the next-generation high-temperature materials to bypass the low–melting point limitation of eutectic alloys and diffusion-dominated softening in conventional superalloys.**

## INTRODUCTION

The emerging hypersonic applications and reusable rocket technologies require exotic hot-end materials having a high strength under high-temperature and high-pressure conditions. Traditional Ni-, W-, and Mo-based solid-solution alloys have been widely applied in service because of their excellent high-temperature strength (*1*–*3*). However, at temperatures above 1373 K, the strengths of these single principal–element alloys decline quickly and are limited by diffusion-dominated softening. Recently, a new class of refractory multiprincipal-element alloys (MPEAs) has been shown to exhibit enhanced high-temperature strength because of their high mixing entropy that stabilizes the microstructure (*4*–*7*). For example, MoNbTaW and MoNbTaWV exhibited engineering compressive yield strengths of above 400 MPa and ultimate strengths of above 470 MPa at 1873 K (*6*, *8*), which were notably higher than that of their metals and dilute alloys counterparts (*2*, *3*). However, these refractory MPEAs still quickly lost strength at 1473 K because of rapid grain coarsening.

To overcome microstructural instability, eutectic alloys with the addition of a second phase are required to stabilize the microstructure at high temperatures, so that the co-strengthening effects of the grain boundary and second phase can be used (*9*, *10*). In addition, wisdom learned from the two-phase ($\gamma/\gamma'$) structures in Ni-based superalloys (*11*, *12*) and directionally solidified NiAl-Mo eutectic composites (*13*, *14*) suggests that eutectic alloys with interwoven fine eutectic microstructures can provide a promising pathway to achieve both high-temperature strength and room-temperature plasticity (*15*, *16*). From a metallurgical point of view, eutectic composition with a relatively low melting point benefits high castability and excellent processability, for example, the directionally solidified NiAl-Mo eutectic alloy. However, directionally solidified NiAl-Mo eutectic alloy is noted to suffer from a weak interface and a low creep resistance of the NiAl matrix and Mo fibers (*13*, *14*). To further enhance the high-temperature strengths, several eutectic MPEAs have been developed, which were demonstrated to achieve excellent chemical and structural stabilities at elevated temperatures (*15*, *17*). However, these eutectic MPEAs are also noted to exhibit insufficient resistance to high temperatures due to relatively low melting points (<1673 K).

Additional efforts were made by incorporating ceramic phase into refractory MPEAs, such as $Mo_{0.5}NbHf_{0.5}ZrTiSi_x$, $Mo_{0.5}NbHfTiV_{0.5}Si_x$, and $C_xHf_{0.25}NbTaW_{0.5}$, to improve the high-temperature strength (*18*–*20*). These refractory MPEAs have been demonstrated to have a good combination of improved high-temperature strength and room-temperature plasticity. Again, the silicide-reinforced MPEA alloys have demonstrated a poor strength of less than 250 MPa at 1473 K, while the $C_xHf_{0.25}NbTaW_{0.5}$ alloys showed microstructural instability with the formation of nanoprecipitates after annealing at 1673 K and recrystallization when compressed at 1473 K.

It has been shown previously that the addition of 0.5Re (molar fraction) to the MoNbTaW MPEA could enhance the alloy's strength and ductility simultaneously (*21*). Inspired by this study, we further introduce high-strength carbide to the $Re_{0.5}MoNbTaW$ to promote the formation of a eutectic structure, as predicted from the quasi-binary M-C (M = Mo, W, Ta, and Nb) phase diagrams, in which a notably eutectic structure composed of concentrated solid-solution phase and carbide is expected to form (*22*–*24*). Therefore, in the current study, we develop refractory metallic-carbide $Re_{0.5}MoNbW(TaC)_x$ (x = 0.8, 0.9, 1.0) eutectic MPEAs with tunable microstructure. The eutectic composition is readily realized by arc-melting a mixture of TaC and $Re_{0.5}MoNbW$. It is noted that the mixing of NbC with $Re_{0.5}MoTaW$ also gives the same alloy composition.

[1]Centre for High-Resolution Electron Microscopy, College of Materials Science and Engineering, Hunan University, Changsha 410082, China. [2]State Key Lab of Advanced Technology for Materials Synthesis and Processing, Wuhan University of Technology, Wuhan 430070, China. [3]State Key Laboratory of Advanced Design and Manufacturing for Vehicle Body, College of Mechanical and Vehicle Engineering, Hunan University, Changsha 410082, China. [4]College of Science and Engineering, City University of Hong Kong, Hong Kong 999077, China. [5]Department of Materials Science and Engineering and Hopkins Extreme Materials Institute, Johns Hopkins University, Baltimore, MD 21218, USA. [6]Department of Materials Science and Engineering, The University of Tennessee, Knoxville, TN 37996, USA. [7]Pico Electron Microscopy Center, College of Materials Science and Engineering, Hainan University, Haikou, Hainan 570228, China.
*Corresponding author. Email: xiandongxu@hnu.edu.cn (X.X); sqqf@263.net (Q.S.); mwchen@jhu.edu (M.C.); tnieh@utk.edu (T.G.N.); jhchen123@hnu.edu.cn (J.C.)

We demonstrate that these alloys can achieve (i) excellent microstructural stability of eutectic $(TaC)_x$ (x = 0.8, 0.9, and 1.0), (ii) exceptional high-temperature strength by the carbide phase, (iii) solid-solution strengthening of the matrix, and (iv) good room-temperature plasticity of the metallic phase. As a result, the designed superrefractory alloy is expected to have superhigh-temperature strength and microstructural stability while maintaining appreciable plasticity at ambient temperature. Our results show that the $(TaC)_x$ (x = 0.8, 0.9, and 1.0) eutectic alloys have a yield strength of up to 1.1 GPa and compressive strength of 2.12 GPa at 1473 K, together with good room-temperature plasticity of ~10%.

## RESULTS

### Microstructures of the as-cast $(TaC)_x$ (x = 0.8, 0.9, 1.0) alloys

$(TaC)_x$ (x=0.8, 0.9, and 1.0) alloys were cast using high-purity powders (see the Supplementary Materials). Scanning electron microscopy (SEM)–backscattered electron (BSE) images (Fig. 1A) and x-ray diffraction (XRD) patterns (fig. S1) of the alloys reveal that a fully eutectic microstructure consisting of the body-centered cubic (BCC) phase (lattice parameter, $a$ = 0.3194 nm) and the NaCl-type face-centered cubic (FCC) carbide phase ($a$ = 0.4414 nm) was observed in $(TaC)_{0.9}$ alloy with a eutectic composition, whereas the primary BCC and primary FCC carbide phases were observed in $(TaC)_{0.8}$ hypoeutectic and $(TaC)_{1.0}$ hypereutectic alloys, respectively. In the SEM images, the grain sizes of the primary BCC and carbide phases in the hypo- and hypereutectic alloys appear larger than that of eutectic colonies. It is noted that the primary phases only appear in the hypo- and hypereutectic compositions.

Quantitative chemical analyses by combining electron probe microanalyzer (EPMA) and energy-dispersive x-ray spectroscopy (table S1 and fig. S2) demonstrate that the BCC phase is a multiprincipal-element phase with a composition of $W_{32.1}Mo_{21.9}Re_{16.7}Ta_{15.8}Nb_{13.5}$, while the FCC carbide phase is also a multicomponent carbide with a composition of $(Nb_{28.6}Ta_{27.7}Mo_{4.4}W_{4.1})_{64.8}C_{35.2}$. Structure analyses by the transmission electron microscopy (TEM) imaging and selected-area electron diffractions (SAED) further confirm the presence of BCC and multicomponent carbide phases, as well as an approximate Kurdjumov-Sachs (K-S) orientation relationship between the BCC phase and the multicomponent carbide, i.e., $(011)_{BCC}//(111)_{carbide}$ and

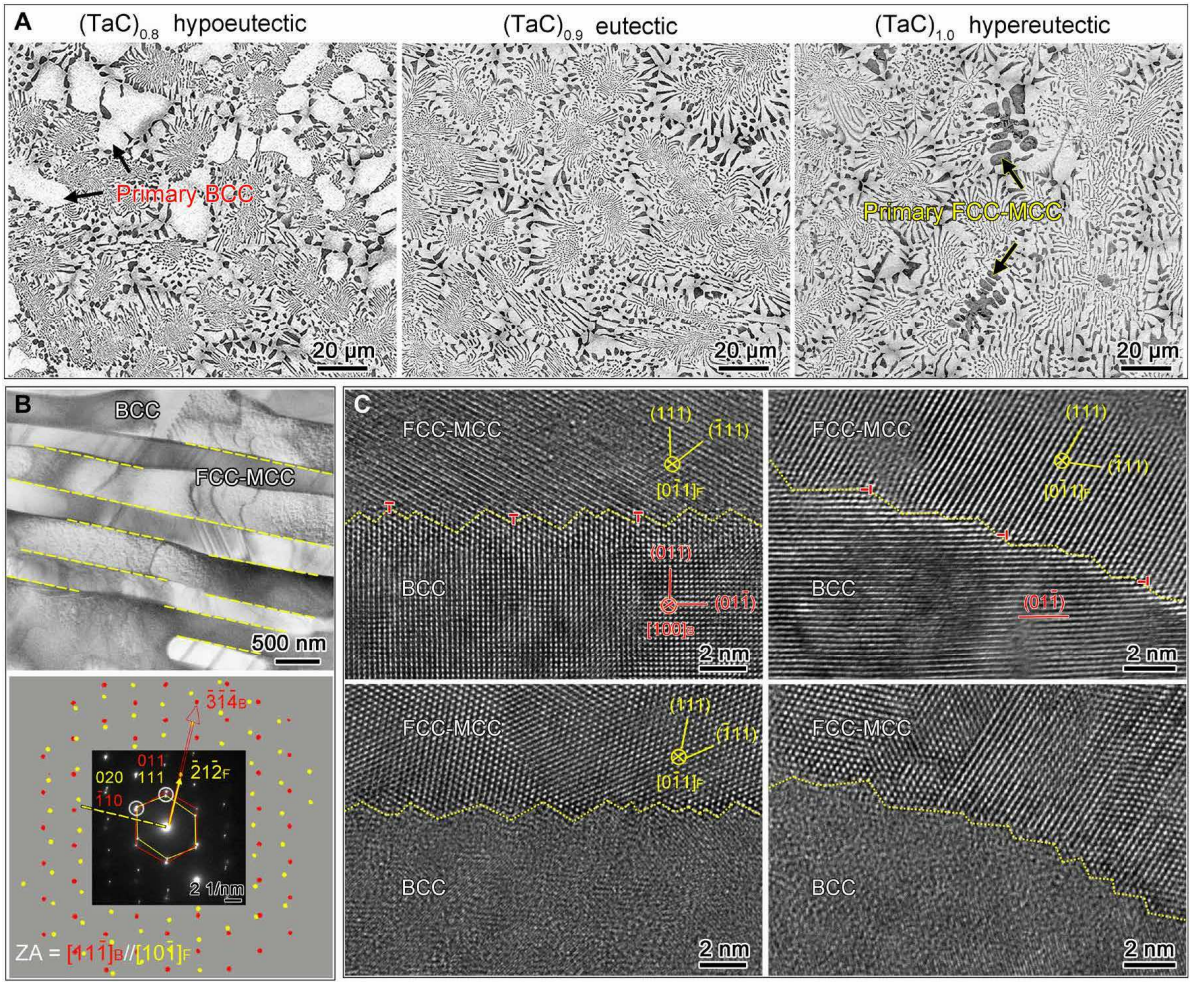


**Fig. 1. Microstructure of the as-cast $(TaC)_x$ (x = 0.8, 0.9, and 1.0) alloys.** (**A**) SEM-BSE images of $(TaC)_x$ (x = 0.8, 0.9, and 1.0)alloys show a fully eutectic microstructure of the $(TaC)_{0.9}$. (**B**) Bright-field TEM image with experimental (inserted) and simulated SAED patterns of the eutectic structure in the $(TaC)_{0.9}$ alloy. (**C**) Edge-on view of two typical BCC/carbide phase interfaces (the bottom images are slightly tilted away from the zone axes of the top images). ZA and subscript letter B refer to zone axes and BCC phase, respectively. Both subscript letter F and FCC-MCC refer to the multicomponent carbide.

$[11\bar{1}]_{BCC}//[10\bar{1}]_{carbide}$, this relationship is defined by the $\{110\}_{BCC}//\{111\}_{carbide}$ and $<111>_{BCC}//<110>_{carbide}$ (Fig. 1B and fig. S2).

To unveil the fine structure of the BCC/carbide interfaces depicted by dash lines from reciprocal space, we simulated single-crystal electron diffraction patterns on the basis of experimental inputs to extrapolate information beyond experimental resolutions. The simulated patterns reveal a relationship defined by $(\bar{3}\,1\,\bar{4})_{BCC}//(\bar{2}1\bar{2})_{carbide}$, as shown by the arrows in Fig. 1B. In the real space, the flat interfaces through aberration-corrected high-resolution TEM by slightly tilting away from the crystal zone axis show a zigzag morphology with visible interfacial dislocations, as depicted by dashed lines in Fig. 1C. The interfaces contain an array of misfit dislocations that accommodate the lattice mismatch between the two phases (*25*, *26*). Theoretically, the zigzag interface is considered an intrinsic structural feature of eutectics with low interfacial energy (*25*–*28*), which is expected to have high thermal and mechanical stabilities against interfacial diffusion and sliding—main contributors for high-temperature softening.

## Compressive properties

Engineering and true compressive stress-strain curves of the $(TaC)_x$ (0.8, 0.9, and 1.0) alloys at 1473 and 298 K are displayed in Fig. 2 (A and B). For comparison, stress-strain curves of the $(TaC)_{0.5}$ hypoeutectic alloy were also included (*29*, *30*). Among $(TaC)_x$ MPEAs, the $(TaC)_{0.9}$ eutectic alloy exhibits the highest 0.2% offset engineering yield strength (1.08 GPa) and compressive strength (2.12 GPa) with a plastic strain of ~22.5% without fracture at 1473 K (Fig. 2A). In contrast to the limited room-temperature plasticity of most MPEAs (*5*, *6*), which soften at $T > 1473$ K, the present $(TaC)_x$ alloys retain a plastic strain even up to 6.7 to 10.2%, suggesting good processability. In particular, the $(TaC)_{0.9}$ alloy exhibits the best strength-plasticity combination with an engineering yield strength of 1.44 GPa, a compressive strength of 2.55 GPa, and a plastic strain of 8.5% at 298 K (Fig. 2B). The compressive properties in the $(TaC)_x$ alloys at 298 and 1473 K demonstrate simultaneous good high-temperature resistance to softening and appreciable plasticity at room temperature. To further investigate the temperature dependence of the compressive properties of the $(TaC)_{0.9}$ alloy, strain-stress curves at temperatures ranging from 298 to 1473 K were acquired and displayed in Fig. 2C. The engineering yield strength and compressive strength values at various temperatures are summarized in Fig. 2 (D and E) and compared with that in the conventional high-temperature alloys. It is evident that the $(TaC)_{0.9}$ MPEA shows substantially higher values of the engineering yield strengths and compressive strengths at high temperatures, as compared with Ni-based superalloys (*6*), NiAl-Mo alloy (*13*), refractory W and Mo alloys (*3*, *31*–*34*), high-strength refractory MPEAs (*6*, *35*–*37*), and $HfMo_{0.5}NbTiV_{0.5}Si_x$ and

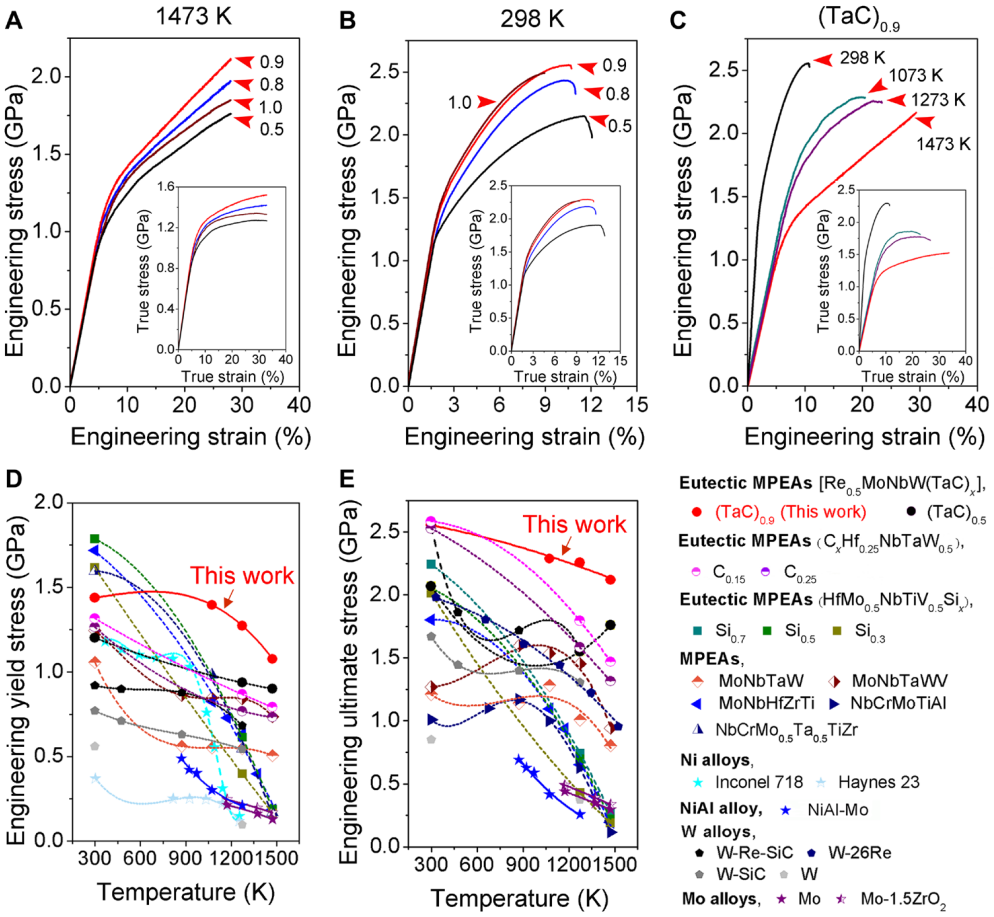


**Fig. 2. Compressive properties of the $(TaC)_x$ (x = 0.8, 0.9, and 1.0) alloys.** (**A** and **B**) Stress-strain curves of the $(TaC)_x$ (x = 0.8, 0.9, and 1.0)alloys at 1473 and 298 K showed high strength and good plasticity. (**C**) Stress-strain curves of the $(TaC)_{0.9}$ alloy at different temperatures. (**D** and **E**) A comparison of the temperature dependence of engineering yield strengths and compressive strengths of the $(TaC)_{0.9}$ with Ni-based alloys, NiAl alloy, W alloys, Mo alloys, and MPEAs shows ultrahigh strength of the $(TaC)_{0.9}$ eutectic alloy.

$C_xHf_{0.25}NbTaW_{0.5}$ eutectic MPEAs (*19*, *20*). It is particularly pointed out that the $(TaC)_{0.9}$ alloy with a eutectic structure exhibits the best high-temperature compressive properties, demonstrating that the refractory multiprincipal-element metal-carbide eutectic microstructure is effective in achieving exceptional high-temperature mechanical properties.

### Postdeformation microstructures

SEM observations were carried out to characterize the postdeformation microstructure of the $(TaC)_x$ alloys after compression at 1473 K (fig. S3). Compared to the as-cast alloy, a notable coarsening of the primary BCC phase was observed in the $(TaC)_{0.8}$ hypoeutectic alloy. By contrast, the $(TaC)_{0.9}$ eutectic alloy shows no discernable microstructural coarsening, suggesting high thermal stability of the eutectic microstructure. Notably, the $(TaC)_{1.0}$ hypereutectic alloy with the excessive primary carbide also shows high thermal stability against microstructure coarsening at the deformation temperatures; this arises from the intrinsic high stability of the carbide phase. However, the excessive primary carbide deteriorates the room-temperature plasticity of the $(TaC)_{1.0}$ hypereutectic alloy as displayed in Fig. 2B.

Electron backscatter diffraction (EBSD) experiments were also conducted to detect changes in both the dislocation density and crystallographic orientation relationship of the $(TaC)_{0.9}$ alloy after deformation (fig. S4). The results reveal an exceedingly low dislocation density in both the BCC and carbide phases before the compression. However, after compression at 298 K, a high density of dislocations evolved in the BCC phase, while no dislocation was detectable in the carbide phase. Dislocation densities in both BCC and carbide phases increase with increasing compression temperature, as demonstrated in the kernel-based local average misorientation (LAM) images. The high-density dislocations revealed by LAM images at all temperatures reside only in the BCC phase and concentrate in the vicinity of BCC/carbide interfaces, suggesting that the relatively soft BCC phase contributes to the plastic deformation and that the phase interfaces can effectively block dislocations gliding. Meanwhile, numerous 60° <111> deformation twins become visible in the carbide phase after compression at 1273 K, and the number of twins increases substantially when samples were compressed at 1473 K, as indicated by arrows in fig. S4C. The formation of these deformation twins is also confirmed by the EBSD analysis of randomly selected two regions (fig. S5) and by the TEM observations (fig. S6).

In addition to the dislocation density changes, crystallographic orientation relationships between the carbide and BCC phases are determined by randomly selecting 16 eutectic colonies from the inverse pole figure maps. The results reveal that 12 of 16 colonies have the approximate K-S orientation relationship, namely, $(011)_{BCC}//(111)_{carbide}$ and $[11\bar{1}]_{BCC}//[10\bar{1}]_{carbide}$, which is in good agreement with the SAED result shown in Fig. 1B. However, no well-defined orientation relationship for the remaining four colonies was detected, indicating that most of the eutectic colonies nearly accommodate the K-S orientation relationship. The K-S orientation relationship was found to retain after compressions at both room and elevated temperatures with a slight deviation of crystal plane angles (fig. S4D), affirming the high thermal and mechanical stabilities of the eutectic structure.

Postdeformation microstructures of the $(TaC)_{0.9}$ alloy deformed at 298, 1073, and 1473 K were further examined using TEM to understand the intrinsic correlation between the microstructure and compressive properties (Fig. 3, A to C). The BCC phase contains a high density of dislocations with a wavy dislocation character after compression at all temperatures, while no visible dislocations are detectable in the carbide phase in the $(TaC)_{0.9}$ alloy compressed at 298 K to 2.55 GPa (Fig. 3A), suggesting that the dislocation nucleation and propagation are hindered at room temperature. The nondeformable carbide phase at 298 K is also supported by the existence of fine cracks frequently observed by TEM and SEM, while the softer BCC lamellae serve as buffers to blunt crack tips and to shield the high local stresses (Fig. 3A and fig. S7). These high-density microcracks act effectively to release local concentrated stresses and improve plasticity (*38*, *39*).

With increasing compression temperature (at 1073 K to 2.29 GPa), the brittle carbide phase in the $(TaC)_{0.9}$ alloy shows numerous full dislocations (Burger's vector <011>$a/2$) and a high density of stacking faults (Fig. 3B), suggesting that a brittle-to-ductile transition takes place in the carbide phase at high temperatures. Further increasing the deformation temperature to 1473 K leads to a further increase in the number of stacking faults (Fig. 3C). The nature of these stacking faults in the carbide phase deformed at 1073 and 1473 K is additionally verified by bright-field TEM imaging, together with the SAED experiments (Fig. 3D). The fine structure of these stacking fault ribbons was analyzed by high-angle annular dark-field aberration-corrected scanning TEM imaging and revealed an alternative stacking of two-/three-layer hexagonal close-packed (HCP; denoted as "*h*") and FCC phase (denoted as "*c*"; Fig. 3E). The presence of the stacking faults with an HCP arrangement indicates deformation-induced FCC-to-HCP transformation, which is attributable to a decrease in stacking fault energies. From an atomistic perspective, the stacking faults occur by the passage of partial dislocations (denoted as "P") at the phase interfaces (Fig. 3, C and F), where the nucleation of both partial dislocations and full dislocations (Frank-Read mode) denoted as "N" takes place because of the high internal stress from the interfacial dislocation pileup, as shown in Fig. 3C.

## DISCUSSION

### Correlation between entropy and the outstanding high-temperature properties

The postcompression microstructure was analyzed by SEM-EBSD and TEM, which revealed a dislocation-dominated deformation in both the BCC and carbide phases up to 1473 K. In general, the high-temperature deformation is governed by diffusion-related mechanisms such as dislocation creep, grain boundary sliding, and interfacial sliding. The fact that high-temperature plasticity was caused by dislocation motion in the $(TaC)_{0.9}$ MPEA suggests that atomic diffusion was effectively suppressed by the high configurational entropies of both multicomponent BCC and carbide phases, and solid-solution strengthening was acting as the effective strengthening mechanism. On the basis of the compositions depicted in table S1, the configurational entropy values for the BCC and carbide phases are calculated to be 1.56*R* and 1.08*R*—both are distinctively larger than those for conventional alloys, which usually only have a value of less than 0.69*R* (where *R* is the gas constant) (*4*). It has been suggested that high configuration entropy may lead to sluggish diffusion in MPEAs (*40*–*42*). For example, a comparison of the tracer diffusion of Ni in pure Ni, ternary CrFeNi, quaternary CoCrFeNi, and quinary CoCrFeMnNi alloys as a function of homologous high

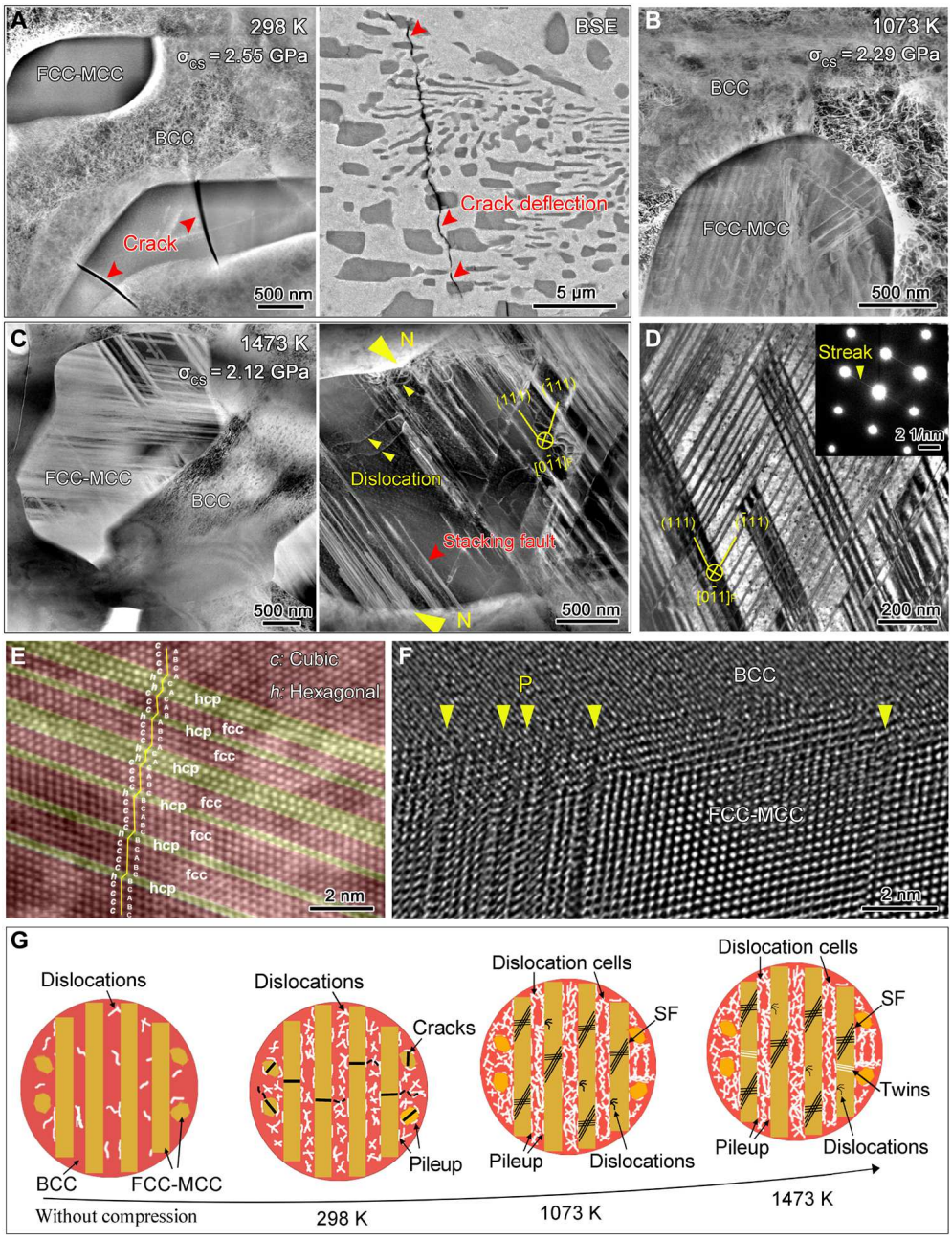


**Fig. 3. TEM analysis of the deformed $(TaC)_{0.9}$ alloy shows the evolution of defects with increasing compression temperatures.** (**A**) 298-K deformed alloy with a compressive strength of 2.55 GPa, (**B**) 1073-K deformed alloy with a compressive strength of 2.29 GPa, and (**C**) 1473-K deformed alloy with a compressive strength of 2.12 GPa. (**D** and **E**) Stacking faults in the 1473-K deformed multicomponent carbide (FCC-MCC). (**F**) A high-resolution TEM image of the phase interface shows the origins of partial dislocations. (**G**) Schematic diagram of defect evolution. SF refers to stacking faults in (G). $\sigma_{CS}$ refers to the compressive strength.

temperature revealed that the diffusion rate of Ni decreases with an increase in the number of elements because of the increased variability of local energy barriers for a diffusion atom (*40*). The sluggish diffusion in the refractory MPEAs is further demonstrated by the fact that the MoNbTaW alloy with a lower entropy value (1.38*R*) is less resilient to the high-temperature deformation as compared to that of the MoNbTaWV alloy with a relatively higher entropy value (1.6*R*) (*6*).

The observation of a high density of dislocations in BCC and stacking faults in the carbide phase after compression above 1073 K (Fig. 3, B and C) conforms with the result of high-temperature plasticity in the $(TaC)_{0.9}$ alloy. The good plasticity of the $(TaC)_{0.9}$ MPEA evidently results from dislocation activities at high temperatures, which can effectively mitigate the stress concentrations at carbide/BCC interfaces to prevent the formation of cracks.

The observed deformation mode for the multicomponent carbide phase after compression at high temperatures occurs dominantly by partial dislocations that generate stacking faults, HCP phase, and deformation twins (Fig. 3, B to F, and figs. S4 to S6). The simultaneous observations of twin and stacking faults at high temperatures

appear to be contradictory, as these faults are not expected to be observed because stacking fault energy could increase with temperatures (*43*, *44*). In general, the carbide phase exhibits a brittle manner, arising from their high Peierls-Nabarro stresses that prevent the activation of dislocations at room temperature. It undergoes a brittle-to-ductile transition at high temperatures as a sufficient number of dislocation slip systems can be thermally activated (*45*, *46*). At high temperatures, therefore, the conventional single-phase carbides (e.g., TaC and NbC) are usually deformed only by perfect dislocation glide on {111} planes (*47*, *48*). The present observation that many stacking faults and deformation twins appear in the multicomponent carbide phase in the $(TaC)_{0.9}$ MPEA supports that the multicomponent carbide has a lower stacking fault energy than those of conventional monocarbides, which leads to the improved fracture toughness of high-entropy carbide (*49*, *50*). Similar to many reported MPEAs, this reduced stacking fault energy is mainly attributable to the chemical effect of the high entropy (*51*), in which the addition of alloying elements can decrease the stacking fault energy and promote plastic deformation by twinning and stacking faults (*44*, *52*). Meanwhile, the formation of deformation twins is considered local stress dependent, which occurs with increasing plastic strains at high temperatures (*53*).

### Interface-stabilized eutectic MPEAs

In comparison with the $(TaC)_{0.8}$ hypoeutectic alloy, which exhibits a rapid coarsening of the primary BCC phase upon high-temperature compression (fig. S3), the highly stable microstructure of the $(TaC)_{0.9}$ fully eutectic alloy is attributable to thermally stable BCC/carbide phase interfaces, in addition to the entropy-stabilized BCC and carbide phases. The improved microstructural stability via the eutectic composition is also reflected by the fact that TaC-free MoNbTaWV MPEA, even with a high-entropy value, exhibits distinct grain coarsening upon deformation at 1073 K (*6*). Therefore, grain boundary and second-phase strengthening play essential roles in the exceptional high-temperature microstructural stability and strength. For coherent/semicoherent interfaces, the continuity of lattice planes across the interfaces can be preserved fully or partially (*54*), and the lattice mismatch between two phases is accommodated by elastic strains or geometrically necessary dislocations. Thus, there is a relatively small interfacial energy, but high elastic strain energy. To verify the nature of the BCC/carbide phase interfaces, the orientation relationship of the as-cast and deformed $(TaC)_{0.9}$ was observed through TEM (Fig. 4). A mismatching degree factor $\overline{\delta^{(hkl)_s}_{(hkl)_n}}$ between the BCC and carbide phases is calculated on the basis of the Bramfitt lattice matching theory (*55*, *56*)

$$\overline{\delta^{(hkl)_s}_{(hkl)_n}} = \sum_{i=1}^{3} \frac{|(d_{[uvw]_s^i}\cos\theta) - d_{[uvw]_n^i}|}{d_{[uvw]_n^i}} \times 100\% \quad (1)$$

where $d_{[uvw]s}$ and $d_{[uvw]n}$ are planar spacings along the $[uvw]_s$ and $[uvw]_n$ of the BCC and carbide phases, and they are derived from the lattice parameters measured by XRD (fig. S8); $h$, $k$, and $l$ are the Miller index; θ is an angle between two crystal planes, and its value is summarized in table S2. The calculated mismatch degree factor of the $(TaC)_{0.9}$ alloy before compression is about 5.70%, which is within the range for a semicoherent interface ($5\% < \delta < 25\%$), consistent with the interfacial structure revealed by aberration-corrected high-resolution TEM shown in Fig. 1C. This mismatch value remains almost unchanged after compression at 298 and 1473 K with a value of 5.51 and 5.68%, and this further validates the high stability of the BCC/carbide phase interfaces, which is expected to stabilize the

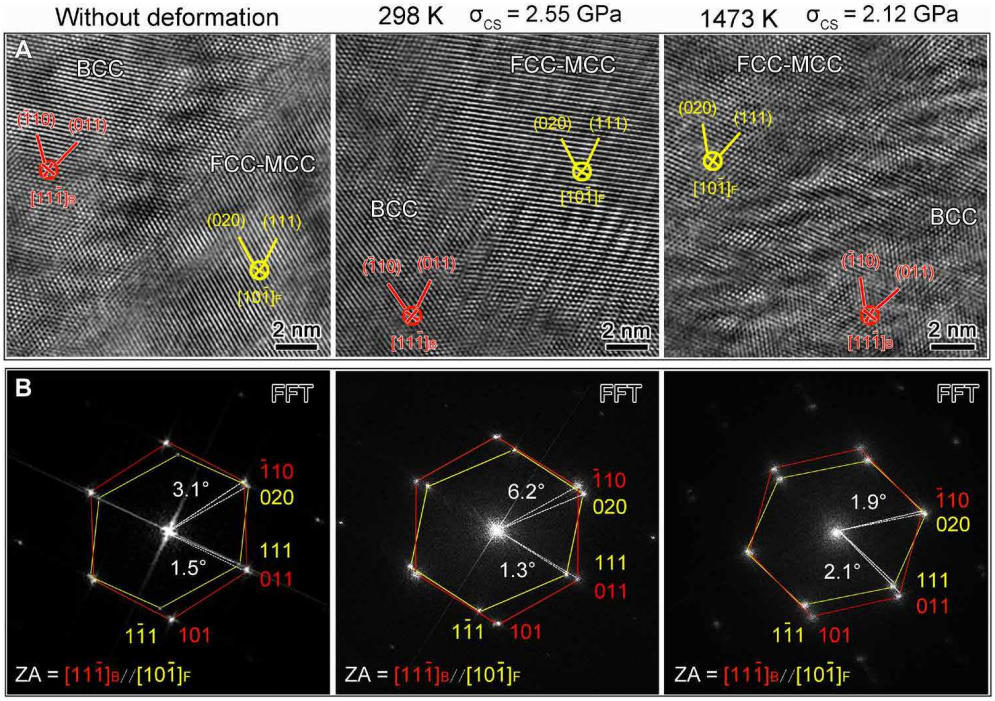


**Fig. 4. Orientation relationship of the as-cast and deformed $(TaC)_{0.9}$ samples through TEM observation.** (**A** and **B**) High-resolution TEM images and the corresponding fast Fourier transform (FFT) patterns of BCC and carbide (FCC-MCC) phases.

eutectic microstructure at high temperatures. The high thermal stability of the interfaces may be associated with the decreased interfacial strain energy at high temperatures through lattice relaxation.

In addition to the high thermal stability of the interfaces, the interlocking configuration of the BCC/carbide phases also plays an essential role in the high-temperature stability of the eutectic microstructure from enlarged diffusion paths along the sluggish multiprincipal-element phase interfaces. Generally, heterogeneous interfaces composed of immiscible materials (e.g., W-$TiC_p$ composite) have superior thermal stability, where the diffusivity is distinctively lower as compared to that of monolithic W (*57*, *58*). As a result, the high-temperature migration of the grain boundary is hindered. For example, in a nanolayered immiscible Cu-Nb composite with the zigzag interface, the microstructure and hardness are stable after annealing up to 773 K (*59*). Meanwhile, the interface between an ordered hard precipitate and a relatively soft matrix acts as the bottleneck to slow down diffusion (*60*), and the BCC/carbide phase interface suppresses climb-controlled grain boundary sliding during creep as compared with those of monocarbides (*47*). For the presently studied eutectic alloy, the combination of the sluggish diffusion resulting from the high entropy effect and the excellent thermal and mechanical stability resulting from metal-carbide semicoherent interfaces contributes to the excellent high-temperature strength and room-temperature plasticity.

In summary, we have developed a novel, fully eutectic carbide–reinforced MPEA with a superb high-temperature strength at 1473 K and excellent microstructural stability. The microstructure consists of an interwoven BCC alloy–FCC carbide layered structure. At high temperatures, the layered carbide skeleton carries the load, and the superb strength arises primarily from solid-solution strengthening, grain boundary strengthening, and second-phase strengthening in the alloy matrix. At room temperature, on the other hand, the alloy layers buffer crack propagation, delay fracture, and promote plasticity. The development of this innovative microstructure offers a new route for the design of high-temperature materials by circumventing the inherent low melting points of traditional eutectic alloys and diffusion-controlled softening in conventional high-temperature alloys.

## MATERIALS AND METHODS

$(TaC)_x$ MPEAs (with a molar ratio of 0.5:1:1:1:*x*) were synthesized via a nonconsumable arc-melting furnace under a high-purity argon atmosphere. Re, Mo, Nb, W, and TaC powders (high-purity of more than 99.9%) were weighed, well mixed, pressed, and then melted to obtain the as-cast MPEA ingots with diameters of Φ 23 to 25 mm and height of about 8 mm. Each MPEA ingot was remelted five times to ensure compositional uniformity. Room-temperature (298 K) compression tests of cylindrical specimens with Φ 2 mm by 4 mm were conducted using an Instron 5966 testing machine at a strain rate of $2 \times 10^{-3}$ $s^{-1}$. The strain was calibrated using an extensometer. High-temperature compression tests of cylindrical specimens with Φ 4 mm by 6 mm were conducted at 1073, 1273, and 1473 K in an argon atmosphere using a Gleeble 2000 thermal simulator with tungsten carbide platens at a strain rate of $1 \times 10^{-3}$ $s^{-1}$. The strain here was calibrated by measuring the initial and final lengths of the compressive specimens. The specimens were compressed to a 28% height reduction or to fracture, whichever happened first.

An x-ray diffractometer with Cu-Kα radiation was used to measure the crystal structure of the MPEAs at 40 kV and 40 mA. SEM (Thermo Fisher Scientific, Helios 5 CX DualBeam) and aberration-corrected (scanning) TEM (S/TEM; Thermo Fisher Scientific, Themis Z) were performed to characterize the microstructure and chemistry. An EPMA was used for measuring chemical compositions. EBSD experiments were performed using SEM (Quanta 200).

## SUPPLEMENTARY MATERIALS

Supplementary material for this article is available at https://science.org/doi/10.1126/sciadv.abo2068

## REFERENCES AND NOTES


1. H. Long, S. Mao, Y. Liu, Z. Zhang, X. Han, Microstructural and compositional design of Ni-based single crystalline superalloys—A review. *J. Alloys Compd.* **743**, 203–220 (2018).
2. S. W. H. Yih, C. T. Wang, *Tungsten: Sources, Metallurgy, Properties, and Applications* (Plenum Press, ed. 3, 1979), p. 168.
3. C. Cui, Y. Gao, S. Wei, G. Zhang, Y. Zhou, X. Zhu, Microstructure and high temperature deformation behavior of the Mo-$ZrO_2$ alloys. *J. Alloys Compd.* **716**, 321–329 (2017).
4. D. B. Miracle, O. N. Senkov, A critical review of high entropy alloys and related concepts. *Acta Mater.* **122**, 448–511 (2017).
5. Y. Zhang, T. T. Zuo, Z. Tang, M. C. Gao, K. A. Dahmen, P. K. Liaw, Z. P. Lu, Microstructures and properties of high-entropy alloys. *Prog. Mater. Sci.* **61**, 1–93 (2014).
6. O. N. Senkov, G. B. Wilks, J. M. Scott, D. B. Miracle, Mechanical properties of $Nb_{25}Mo_{25}Ta_{25}W_{25}$ and $V_{20}Nb_{20}Mo_{20}Ta_{20}W_{20}$ refractory high entropy alloys. *Intermetallics* **19**, 698–706 (2011).
7. R. R. Eleti, T. Bhattacharjee, A. Shibata, N. Tsuji, Unique deformation behavior and microstructure evolution in high temperature processing of HfNbTaTiZr refractory high entropy alloy. *Acta Mater.* **171**, 132–145 (2019).
8. O. N. Senkov, G. B. Wilks, D. B. Miracle, C. P. Chuang, P. K. Liaw, Refractory high-entropy alloys. *Intermetallics* **18**, 1758–1765 (2010).
9. B. Cao, T. Yang, W.-H. Liu, C. T. Liu, Precipitation-hardened high-entropy alloys for high-temperature applications: A critical review. *MRS Bull.* **44**, 854–859 (2019).
10. J. Y. He, H. Wang, Y. Wu, X. J. Liu, T. G. Nieh, Z. P. Lu, High-temperature plastic flow of a precipitation-hardened FeCoNiCr high entropy alloy. *Mater. Sci. Eng. A* **686**, 34–40 (2017).
11. M. Pröbstle, S. Neumeier, P. Feldner, R. Rettig, H. E. Helmer, R. F. Singer, M. Göken, Improved creep strength of nickel-base superalloys by optimized γ/γ′ partitioning behavior of solid solution strengthening elements. *Mater. Sci. Eng. A* **676**, 411–420 (2016).
12. J. Xu, H. Gruber, R. Boyd, S. Jiang, R. L. Peng, J. J. Moverare, On the strengthening and embrittlement mechanisms of an additively manufactured Nickel-base superalloy. *Materialia* **10**, 100657 (2020).
13. H. Bei, E. P. George, Microstructures and mechanical properties of a directionally solidified NiAl-Mo eutectic alloy. *Acta Mater.* **53**, 69–77 (2005).
14. L. Hu, W. Hu, G. Gottstein, S. Bogner, S. Hollad, A. Buhrig-Polaczek, Investigation into microstructure and mechanical properties of NiAl-Mo composites produced by directional solidification. *Mater. Sci. Eng. A* **539**, 211–222 (2012).
15. Y. Lu, Y. Dong, H. Jiang, Z. Wang, Z. Cao, S. Guo, T. Wang, T. Li, P. K. Liaw, Promising properties and future trend of eutectic high entropy alloys. *Scripta Mater.* **187**, 202–209 (2020).
16. Z. Y. Ding, Q. F. He, Q. Wang, Y. Yang, Superb strength and high plasticity in laves phase rich eutectic medium-entropy-alloy nanocomposites. *Int. J. Plast.* **106**, 57–72 (2018).
17. F. He, Z. Wang, X. Shang, C. Leng, J. Li, J. Wang, Stability of lamellar structures in $CoCrFeNiNb_x$ eutectic high entropy alloys at elevated temperatures. *Mater. Des.* **104**, 259–264 (2016).
18. N. N. Guo, L. Wang, L. S. Luo, X. Z. Li, R. R. Chen, Y. Q. Su, J. J. Guo, H. Z. Fu, Microstructure and mechanical properties of refractory high entropy $(Mo_{0.5}NbHf_{0.5}ZrTi)_{BCC}/M_5Si_3$ in-situ compound. *J. Alloys Compd.* **660**, 197–203 (2016).
19. Y. Liu, Y. Zhang, H. Zhang, N. Wang, X. Chen, H. Zhang, Y. Li, Microstructure and mechanical properties of refractory $HfMo_{0.5}NbTiV_{0.5}Si_x$ high-entropy composites. *J. Alloys Compd.* **694**, 869–876 (2017).
20. S. Wu, D. Qiao, H. Zhang, J. Miao, H. Zhao, J. Wang, Y. Lu, T. Wang, T. Li, Microstructure and mechanical properties of CxHf0.25NbTaW0. Refractory high-entropy alloys at room and high temperatures. *J. Mater. Sci. Technol.* **97**, 229–238 (2022).
21. J. Zhang, Y. Hu, Q. Wei, Y. Xiao, P. Chen, G. Luo, Q. Shen, Microstructure and mechanical properties of $Re_xNbMoTaW$ high-entropy alloys prepared by arc melting using metal powders. *J. Alloys Compd.* **827**, 154301 (2020).

22. E. Rudy, S. Windisch, K. L. Brukl, "Ternary phase equilibria in transition metal boron-carbon-silicon systems" (Technical Report AFML-TR-65-2, part II, vol. XVII, Aerojet-General Corp Sacramento Calif Materials Research Lab, 1967).
23. E. Rudy, "Ternary phase equilibria in transition metal-boron-carbon-silicon systems" (Technical Report AFML-TR-65-2, part II, vol. VII, Aerojet-General Corp Sacramento Calif Materials Research Lab, 1966).
24. C. E. Brukl, "Phase equilibria investigation of binary, ternary, and higher order systems" (Technical Report AFML-TR-69-117, part IV, Aerojet-General Corp, 1969).
25. S. Zheng, I. J. Beyerlein, J. S. Carpenter, K. Kang, J. Wang, W. Han, N. A. Mara, High-strength and thermally stable bulk nanolayered composites due to twin-induced interfaces. *Nat. Commun.* **4**, 1696 (2013).
26. K. Kang, J. Wang, I. J. Beyerlein, Atomic structure variations of mechanically stable fcc-bcc interfaces. *J. Appl. Phys.* **111**, 053531 (2012).
27. S. Zheng, J. S. Carpenter, R. J. McCabe, I. J. Beyerlein, N. A. Mara, Engineering interface structures and thermal stabilities via SPD processing in bulk nanostructured metals. *Sci. Rep.* **4**, 4226 (2014).
28. T. Xiong, W. Yang, S. Zheng, Z. Liu, Y. Lu, R. Zhang, Y. Zhou, X. Shao, B. Zhang, J. Wang, F. Yin, P. K. Liaw, X. Ma, Faceted Kurdjumov-Sachs interface-induced slip continuity in the eutectic high-entropy alloy, $AlCoCrFeNi_{2.1}$. *J. Mater. Sci. Technol.* **65**, 216–227 (2021).
29. Q. Wei, Q. Shen, J. Zhang, Y. Zhang, G. Luo, L. Zhang, Microstructure evolution, mechanical properties and strengthening mechanism of refractory high-entropy alloy matrix composites with addition of TaC. *J. Alloys Compd.* **777**, 1168–1175 (2019).
30. Q. Wei, G. Luo, R. Tu, J. Zhang, Q. Shen, Y. Cui, Y. Gui, A. Chiba, High-temperature ultra-strength of dual-phase $Re_{0.5}MoNbW(TaC)_{0.5}$ high-entropy alloy matrix composite. *J. Mater. Sci. Technol.* **84**, 1–9 (2021).
31. K. Kang, R. Tu, G. Luo, J. Zhang, J. Zhu, Q. Shen, L. Zhang, Mechanical, electrical and thermal properties at elevated temperature of W-Si-C multi-phase composite prepared by arc-melting. *Int. J. Refract. Met. Hard Mater.* **75**, 101–106 (2018).
32. K. Kang, R. Tu, G. Luo, J. Zhang, J. Zhu, Q. Shen, L. Zhang, Synergetic effect of Re alloying and SiC addition on strength and toughness of tungsten. *J. Alloys Compd.* **767**, 1064–1071 (2018).
33. K. Kang, "Preparation, structure control and performance study of W-Re-Si-C composites by arc melting," thesis, Wuhan University of Technology (2018).
34. T. G. Nieh, J. Wadsworth, "Recent advances and developments in refractory alloys" (Technical Report Conf-931108-90, Materials Research Society, 1993).
35. N. N. Guo, L. Wang, L. S. Luo, X. Z. Li, Y. Q. Su, J. J. Guo, H. Z. Fu, Microstructure and mechanical properties of refractory MoNbHfZrTi high-entropy alloy. *Mater. Design* **81**, 87–94 (2015).
36. O. N. Senkov, C. F. Woodward, Microstructure and properties of a refractory $NbCrMo_{0.5}Ta_{0.5}TiZr$ alloy. *Mater. Sci. Eng. A* **529**, 311–320 (2011).
37. H. Chen, A. Kauffmann, B. Gorr, D. Schliephake, C. Seemuller, J. N. Wagner, H.-J. Christ, M. Heilmaier, Microstructure and mechanical properties at elevated temperatures of a new Al-containing refractory high-entropy alloy Nb-Mo-Cr-Ti-Al. *J. Alloys Compd.* **661**, 206–215 (2016).
38. P. Shi, R. Li, Y. Li, Y. Wen, Y. Zhong, W. Ren, Z. Shen, T. Zheng, J. Peng, X. Liang, P. Hu, N. Min, Y. Zhang, Y. Ren, P. K. Liaw, D. Raabe, Y.-D. Wang, Hierarchical crack buffering triples ductility in eutectic herringbone high-entropy alloys. *Science* **373**, 912–918 (2021).
39. M. Koyama, Z. Zhang, M. Wang, D. Ponge, D. Raabe, K. Tsuzaki, H. Noguchi, C. C. Tasan, Bone-like crack resistance in hierarchical metastable nanolaminate steels. *Science* **355**, 1055–1057 (2017).
40. S. V. Divinski, O. A. Lukianova, G. Wilde, A. Dash, N. Esakkiraja, A. Paul, High-entropy alloys: Diffusion, encyclopedia of materials metals and alloys. **2**, 402–416 (2022).
41. C. Ng, S. Guo, J. Luan, S. Shi, C. T. Liu, Entropy-driven phase stability and slow diffusion kinetics in an $Al_{0.5}CoCrCuFeNi$ high entropy alloy. *Intermetallics* **31**, 165–172 (2012).
42. L. Zhang, Y. Duan, D. Crespo, E. Pineda, T. Wada, H. Kato, J.-M. Pelletier, J. Qiao, Identifying the high entropy characteristic in La-based metallic glasses. *Appl. Phys. Lett.* **119**, 051905 (2021).
43. D. Molnár, X. Sun, S. Lu, W. Li, G. Engberg, L. Vitos, Effect of temperature on the stacking fault energy and deformation behaviour in 316L austenitic stainless steel. *Mater. Sci. Eng. A* **759**, 490–497 (2019).
44. B. Zhao, P. Huang, L. Zhang, S. Li, Z. Zhang, Q. Yu, Temperature effect on stacking fault energy and deformation mechanisms in titanium and titanium-aluminium alloy. *Sci. Rep.* **10**, 3086 (2020).
45. G. E. Hollox, R. E. Smallman, Plastic behavior of titanium carbide. *J. Appl. Phys.* **37**, 818–823 (1966).
46. H. Yu, "Stacking faults in the transition metal carbides and nitrides: Stability and mechanical properties," thesis, Drexel University (2017).
47. C. Kim, G. Gottstein, D. S. Grummon, Plastic flow and dislocation structures in tantalum carbide: Deformation at low and intermediate homologous temperatures. *Acta Metall. Mater.* **42**, 2291–2301 (1994).
48. D. J. Rowcliffe, G. E. Hollox, Hardness anisotropy, deformation mechanisms and brittle-to-ductile transition in carbide. *J. Mater. Sci.* **6**, 1270–1276 (1971).
49. T. J. Harrington, J. Gild, P. Sarker, C. Toher, C. M. Rost, O. F. Dippo, C. McElfresh, K. Kaufmann, E. Marin, L. Borowski, P. E. Hopkins, J. Luo, S. Curtarolo, D. W. Brenner, K. S. Vecchio, Phase stability and mechanical properties of novel high entropy transition metal carbides. *Acta Mater.* **166**, 271–280 (2019).
50. Z. Wang, Z.-T. Li, S.-J. Zhao, Z. G. Wu, High-entropy carbide ceramics: A perspective review. *Tungsten* **3**, 131–142 (2021).
51. S. Zhao, G. M. Stocks, Y. Zhang, Stacking fault energies of face-centered cubic concentrated solid solution alloys. *Acta Mater.* **134**, 334–345 (2017).
52. L. Ma, Z. Wang, J. Huang, G. Huang, M. Xue, P. Tang, T. Fan, Effect of alloying elements on stacking fault energies and twinnabilities in high-entropy transition-metal carbides. *J. Am. Ceram. Soc.* **104**, 6521–6532 (2021).
53. J. T. Fan, L. J. Zhang, P. F. Yu, M. D. Zhang, G. Li, P. K. Liaw, R. P. Liu, A novel high-entropy alloy with a dendrite-composite microstructure and remarkable compression performance. *Scripta Mater.* **159**, 18–23 (2019).
54. J. H. Chen, E. Costan, M. A. van Huis, Q. Xu, H. W. Zandbergen, Atomic pillar-based nanoprecipitates strengthen AlMgSi alloys. *Science* **312**, 416–419 (2006).
55. B. L. Bramfitt, The effect of carbide and nitride additions on the heterogeneous nucleation behavior of liquid iron. *Metall. Trans.* **1**, 1987–1995 (1970).
56. C. Yang, L. M. Kang, X. X. Li, W. W. Zhang, D. T. Zhang, Z. Q. Fu, Y. Y. Li, L. C. Zhang, E. J. Lavernia, Bimodal titanium alloys with ultrafine lamellar eutectic structure fabricated by semi-solid sintering. *Acta Mater.* **132**, 491–502 (2017).
57. G.-M. Song, Y.-J. Wang, Y. Zhou, Thermomechanical properties of TiC particle-reinforced tungsten composites for high temperature applications. *Int. J. Refract. Met. Hard Mater.* **21**, 1–12 (2003).
58. W. Xu, B. Zhang, X. Y. Li, K. Lu, Suppressing atomic diffusion with the Schwarz crystal structure in supersaturated Al-Mg alloys. *Science* **373**, 683–687 (2021).
59. Q. An, W. Yang, B. Liu, S. J. Zheng, Interface effects on the properties of Cu-Nb nanolayered composites. *J. Mater. Res.* **35**, 2684–2700 (2020).
60. A. J. Ardell, V. Ozolins, Trans-interface diffusion-controlled coarsening. *Nat. Mater.* **4**, 309–316 (2005).



**Acknowledgments**

**Funding:** This project was funded by China Postdoctoral Science Foundation grant 2021M701135 (to Q.W.); Excellent Postdoctoral Innovative Talents Program of Hunan Province grant 2021RC2043 (to Q.W.); National Natural Science Foundation of China grant 52001120 (to X.X.); the Fundamental Research Funds for the Central Universities grant 531118010450 (to X.X.); State Key Laboratory of Advanced Metals and Materials grant 2021-Z09, University of Science and Technology Beijing, and the State Key Laboratory of Powder Metallurgy, Central South University, Changsha, China (to X.X.); State Key Program of the National Natural Science Foundation of China grant 51932006 (to Q.S.); National Key R&D Program of China grant 2021YFB3802300 (to G.L.); National Natural Science Foundation grant 52171045 (to J.Z.); the Hong Kong Government through Structural-Material Development Fund (SMDF) grant 9360160 (to C.T.L.); National Natural Science Foundation of China grant 51871092 (to J.L.); National Natural Science Foundation of China grant 12072109 (to Q.F.); U.S. National Science Foundation grant DMR-1804320 (to M.C.); U.S. National Science Foundation grant DMR-1408722 (to T.G.N.); and National Natural Science Foundation of China grant 51831004 (to J.C.). **Author contributions:** X.X., Q.S., C.T.L., M.C., T.G.N., and J.C. designed and supervised the research. Q.W., G.L., and J.Z. prepared samples and conducted mechanical tests. Q.W. and X.X. carried out TEM. Q.W. performed an EBSD analysis. J.L. and Q.F. performed theoretical simulations. Q.W., X.X., and J.C. analyzed the data, prepared the figures, and wrote the draft manuscript. All authors reviewed and contributed to the final manuscript. **Competing interests:** The authors declare that they have no competing interests. **Data and materials availability:** All data needed to evaluate the conclusions in the paper are present in the paper and/or the Supplementary Materials.

Submitted 20 January 2022
Accepted 25 May 2022
Published 8 July 2022
10.1126/sciadv.abo2068

ScienceAdvances

# Metal-carbide eutectics with multiprincipal elements make superrefractory alloys

Qinqin Wei, Xiandong Xu, Qiang Shen, Guoqiang Luo, Jian Zhang, Jia Li, Qihong Fang, Chain-Tsuan Liu, Mingwei Chen, Tai-Gang Nieh, and Jianghua Chen

*Sci. Adv.*, **8** (27), eabo2068.
DOI: 10.1126/sciadv.abo2068